Solar RRL

WILEY VCH

Solar RRL

RESEARCH ARTICLE OPEN ACCESS

Novel Earth-Abundant Cu and Fe-Based Chalcogenide Cocatalysts for Photocatalytic Hydrogen Evolution

Judith Zander[1] | Roland Marschall[1,2]

[1]Department of Chemistry, University of Bayreuth, Bayreuth, Germany | [2]Bavarian Center for Battery Technology (BayBatt), University of Bayreuth, Bayreuth, Germany

Correspondence: Roland Marschall (roland.marschall@uni-bayreuth.de)

Received: 9 May 2025 | **Accepted:** 16 June 2025

Funding: University of Bayreuth

Keywords: earth-abundant cocatalysts | ferrites | hydrogen evolution reaction | photocatalysis

ABSTRACT

While photocatalysis offers an attractive route toward the sustainable production of hydrogen and other green fuels, significant improvements in efficiency and reduction of production costs are still needed. Traditionally, noble metal cocatalysts are used to increase the activity and selectivity of a photocatalyst. In this work, we systematically investigate different nanomaterials based on the abundant and inexpensive elements Cu and Fe as cocatalysts on TiO_2 (P25) for the photocatalytic hydrogen evolution reaction under simulated sunlight as well as under UV irradiation. All the investigated Cu and Fe sulfides/oxides can be obtained *via* a simple and fast microwave-assisted synthesis. In addition, we show how further modifications, such as partial oxidation of the sulfides or doping of $CuFe_2O_4$ with Ni, can have a tremendous effect on the performance as a cocatalyst, increasing the activity by a factor of more than 15 compared to pristine TiO_2 and by a factor of almost 6 compared to TiO_2 equipped with undoped $CuFe_2O_4$ under AM 1.5G simulated sunlight. Under UV irradiation, an H_2 evolution rate of more than 2.3 mmol h^{-1} was achieved. Thus, this work opens a new design platform for the synthesis of earth-abundant cocatalysts for noble metal substitution in photocatalysis.

1 | Introduction

In the context of climate change and an increasing demand for green energy, hydrogen (H_2) is anticipated to assume a pivotal role in a sustainable future. Green H_2 can be produced via water electrolysis. Nevertheless, the cost of the produced H_2 remains considerably higher than that of H_2 obtained through conventional steam reforming. Furthermore, neither the available resources for noble metal-based catalysts (commonly Pt on the cathode and IrO_2 on the anode site) nor the generated renewable electricity is sufficient to sustain H_2 production at a scale that would allow for a complete replacement of fossil-fuel based technologies at an affordable cost in the near future [1, 2]. Photocatalysis represents a promising avenue for solar-to-chemical energy conversion, offering the potential for on-site conversion of solar energy into chemical energy. Nevertheless, the current efficiencies attained, even in the production of H_2, remain relatively low. The addition of noble metal cocatalysts, which are incorporated in nonnegligible amounts, serves to enhance charge extraction and overall conversion efficiencies. However, this practice also contributes to the overall system cost [3, 4]. These findings underscore the necessity for the continued development of not only efficient photocatalysts but also earth-abundant cocatalysts.

This subject has only recently begun to emerge as a topic of interest within the field of photocatalysis. A great deal can be learned from electrocatalysis, however, where the search for earth-abundant catalysts has been pursued extensively over the past few decades [5, 6]. For the oxygen evolution reaction (OER), mainly Ni-Fe-based materials, or cobalt oxides have

emerged as promising catalyst materials [7–9]. On the hydrogen evolution reaction (HER) site, MoS_2 remains one of the most active, earth-abundant catalysts [6]. Other transition metal sulfide and oxide catalysts have shown promising activities as well, though. Binary Fe- and Ni-sulfides are among the materials investigated as potential replacements for noble metal HER catalysts, also owing to their commonly improved conductivity compared to their oxidic counterparts [10]. Thus, e.g., Faber et al. investigated NiS_2, CoS_2, and FeS_2 as electrocatalysts for the HER [11]. NiFe-based sulfides and phosphides have also shown promise, although a (partial) transformation to oxyhydroxide or oxysulfide species is commonly observed [12]. Both ternary NiFe- and CoFe-sulfides exhibit very high activities for electrochemical HER [13–16].

Ni-, Co-, Cu-, Mo-, and Fe-based cocatalysts have been tested as replacement for commonly used noble metals such as Pt, Pd, or Rh in photocatalysis, as well. Examples include metals and alloys, oxides, sulfides, phosphides, or carbides [17–22]. Ran et al. showed how $Ni(OH)_2$ is especially promising if used in combination with $Zn_xCd_{1-x}S$. This study also demonstrated how the interplay of photo- and cocatalyst is crucial for the overall performance [23]. NiS was shown to be an effective cocatalyst on C_3N_4, while NiS_xO_y was employed as a catalyst layer on np-Si photocathodes [24, 25]. Similarly, a 5 wt% CuS-5 wt% NiS composite cocatalyst has been reported [26]. FeS_2 was used by Kuo et al. in a heterojunction with TiO_2, wherein electron transfer from FeS_2 to TiO_2 was proposed [27]. It has also been directly employed as photocatalyst itself in a comparative study with CuS and NiS_2 [28]. Another promising candidate for both electrochemical and photocatalytic/photoelectrochemical HER besides oxide or sulfide materials is CoP [29–31].

Iron-based spinel oxides are well known for their potential as water oxidation catalysts, especially $NiFe_2O_4$ and $CoFe_2O_4$ [32, 33]. They can, however, also catalyze the HER. Thus, we have previously shown that especially $CuFe_2O_4$ is a decent HER catalyst in alkaline media [34, 35]. One of the factors limiting their performance is the poor conductivity of spinel oxides. In contrast, thiospinels display markedly enhanced conductivity and have demonstrated considerable potential for electrochemical HER and OER applications [14, 15, 36]. We previously demonstrated Ni_2FeS_4 as a promising replacement of noble metal cocatalysts [37]. In this study, we investigate the use of Fe- and Cu-based oxide and sulfide materials as cocatalysts on P25 TiO_2. Despite its oxidic nature and limiting conductivity, $CuFe_2O_4$ is shown to be an efficient cocatalyst under both simulated sunlight and UV irradiation. The process of Ni-doping and in situ reduction is crucial for increasing the amount of reduced Cu-species, which significantly improves the overall activity. It is noteworthy that all of the utilized earth-abundant cocatalysts can be synthesized rapidly via microwave-assisted techniques, with the complete reaction occurring within 15 min at approximately 200°C. The resulting chalcogenides are in nanoparticulate form, which allows for a fine, homogeneous distribution over and intimate contact with the photocatalyst. Furthermore, the reduction in particle size has a significant impact on conductivity, as charge carriers only have to travel short distances through the material.

2 | Results

2.1 | Ferrites

Since Ni, Co, Cu, and Fe are all earth-abundant transition metals with established ability to catalyze the HER, we tested $NiFe_2O_4$, $CoFe_2O_4$, and $CuFe_2O_4$ as cocatalysts on P25 at loadings ranging from 1 to 10 wt%. The synthesis of $NiFe_2O_4$ and $CoFe_2O_4$ was conducted via a nonaqueous microwave synthesis in rac-1-phenylethanol, as previously reported (200°C, 30 min) [33, 38]. Similarly, $CuFe_2O_4$ was obtained via a microwave synthesis approach, utilizing ethylene glycol/water mixtures and synthesis conditions of 15 min at 175°C, as previously reported [39]. The obtained ferrite nanocrystals were utilized without undergoing any post-synthetic treatment. While the nonaqueous route has been demonstrated to yield particles with an average diameter of approximately 4 nm, the $CuFe_2O_4$ nanoparticles exhibit a diameter of approximately 17 nm [33, 39].

The spinel cocatalysts were loaded onto TiO_2 by physical mixing involving grinding in *i*-propanol for 10 min. This was followed by annealing for 2 h at 200°C. The constituents were mixed in different ratios. The X-ray diffraction (XRD) patterns, Raman spectra, and IR spectra can be found in the Supporting Information (Figures S1 and S2). Subsequently, the resulting composites were utilized for the photocatalytic HER in 10 vol% aqueous methanol solutions under 1 sun light irradiation (Figure 1a). The decoration of P25 with $NiFe_2O_4$ resulted in a decrease in the H_2 evolution rate compared to pristine P25, which was due to a shadowing effect by the dark-brown ferrite in combination with a lowering of the active mass. In contrast, both $CoFe_2O_4$ and $CuFe_2O_4$ were able to effectively increase the HER activity. In both cases, the performance was optimal at a low mass loading of 1 wt%, which is indicative of a cocatalyst effect. This suggests that electrons are extracted from the ferrite and that protons are converted to H_2 on the surface of the spinel ferrite. The incorporation of 1 wt% of $CuFe_2O_4$ led to an enhancement in activity by approximately 440% in comparison to the pristine TiO_2 P25.

Next, the performance of TiO_2 P25 loaded with 5 wt% of the different spinel ferrites was evaluated under light irradiation from a mercury immersion lamp operated at 500 W. This high light intensity can be assumed to lead to higher concentrations of excited charge carriers in the photocatalyst, as TiO_2 mainly absorbs UV light (Figure 1b). It is noteworthy that the incorporation of a spinel ferrite into the TiO_2 photocatalyst led to a prominent activity enhancement under these conditions. The least active $NiFe_2O_4$-decorated sample exhibited an impressive activity of 880 µmol h^{-1}, while the one with $CuFe_2O_4$ demonstrated an exceptional production of 2.3 mmol h^{-1} of H_2 - a value comparable to that observed in our previous studies on Ni_2FeS_4 [37]. Conversely, the oxides are presumed to be more stable and more readily synthesizable than the sulfides. The markedly disparate behavior under UV compared to solar irradiation suggests the presence of a distinct mechanism governing charge migration and conversion. It is noteworthy that pure $CuFe_2O_4$ also demonstrated some activity under these conditions, which is similar to what was previously observed for Ni_2FeS_4. Therefore, it can be postulated that the spinel ferrites in conjunction with TiO_2 P25 may function as a heterojunction in the context of UV irradiation, thereby enhancing the charge separation. Furthermore,

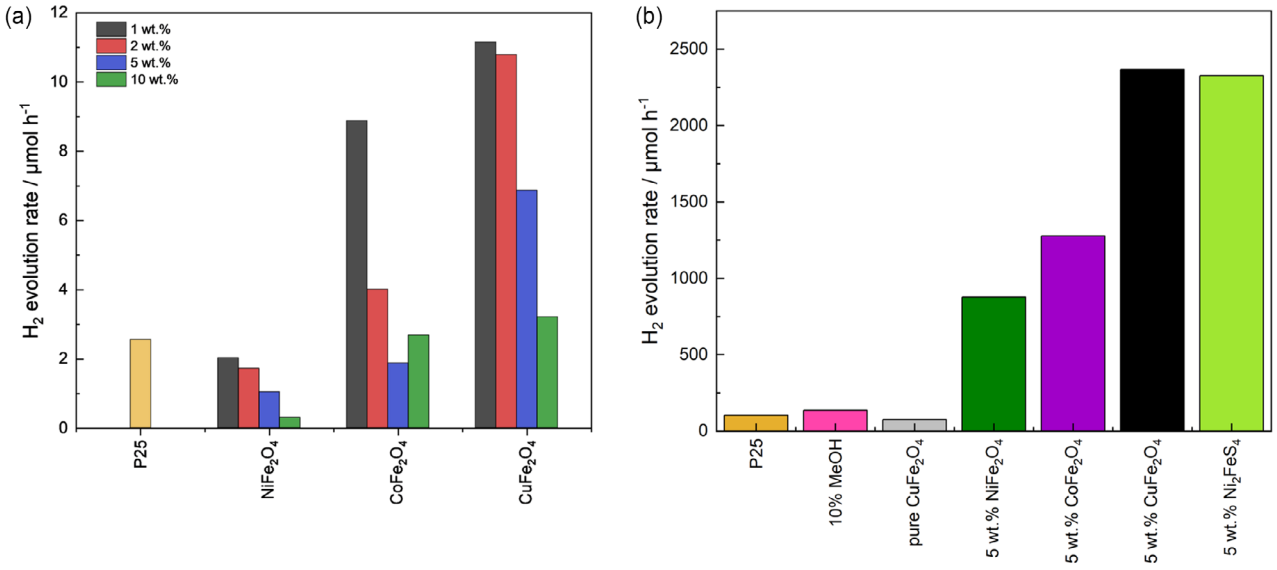

FIGURE 1 | HER using spinel ferrites as cocatalysts on P25. (a) HER under 1sun light irradiation. (b) HER under 500 W Hg irradiation for a cocatalyst loading of 5 wt%. The bars depict the maximum in the H_2 evolution rate observed over the course of 5 h. The performance of Ni_2FeS_4 for comparison is taken from a previous study [37].

the oxide may undergo partial reduction under these conditions, which would account for the enhanced performance and fundamentally distinct behavior, particularly in the case of $NiFe_2O_4$.

2.2 | Modification of the $CuFe_2O_4$ cocatalyst

Given that $CuFe_2O_4$ was identified as the most suitable spinel ferrite cocatalyst, further experiments were conducted to gain deeper insights into the performance and the underlying mechanisms of activity enhancement with this material. For the spinel oxide to act as a cocatalyst, it is advisable to reduce the loading to the greatest extent possible. Accordingly, additional composites were prepared with $CuFe_2O_4$ loadings of 0.5 and 0.25 wt%, and their performance was evaluated under solar irradiation. The UV/vis/NIR spectra indicate that light absorption is slightly improved in the composite materials, particularly in the 300–350 nm range, due to the absorption properties of $CuFe_2O_4$ (Figure S3). By reducing the mass loading of $CuFe_2O_4$, the activity could be further increased to almost 16 µmol h^{-1} for a very low material loading of 0.25 wt% (Figure 2a). This very low material loading is supporting the effect of $CuFe_2O_4$ acting as a cocatalyst in contrast to forming a heterojunction. At such low loading, the ferrite can be assumed to be finely dispersed as nanoparticles over TiO_2, which decreases the importance of bulk properties, such as low conductivity and band positions. The excess of charge carriers generated in TiO_2 likely results in a tunneling of electrons to the ferrite electrocatalyst, on which the HER proceeds. It is noteworthy that the shape of the H_2 evolution curve over time varies with the mass loading. For higher loadings, the maximum activity was reached during the initial period, whereas a gradual increase in activity was observed for loadings below 1 wt%. At low loadings, the agglomeration of $CuFe_2O_4$ is minimized, as is the shadowing of TiO_2. Furthermore, a gradual activation of the material, for example via partial reduction, is likely and can proceed much more efficiently at lower loadings, without impeding the reduction of protons/water to a significant extent. Agglomeration of $CuFe_2O_4$ also increases two very important factors: (1) the importance of bulk properties, since charges have to be transferred through multiple ferrite particles and (2) the relative ratio of excited charge carriers in $CuFe_2O_4$ compared to in TiO_2. While at low loadings charge excitation in $CuFe_2O_4$ is negligible, facilitating transfer of excess electrons to the cocatalyst, at high loadings accumulation of excited electrons in the conduction band of $CuFe_2O_4$ may shift quasi-Fermi levels, and prevent efficient transfer from TiO_2. The Raman and IR spectra, regardless of the loading, only exhibit the anticipated peaks for TiO_2 (Figure S3).

It is noteworthy that the behavior differs markedly under intense UV irradiation (500 W Hg), with a loading of 5 wt% exhibiting significantly higher activity compared to both lower and higher loadings. Another interesting observation is the remarkable stability of $CuFe_2O_4$ activity at low loadings, which contrasts with the initial activation period observed at higher loadings (5 and 10 wt%). For a 5 wt% loading, the activity exhibits a subsequent enhancement, whereas for 10 wt% the activity declines after initially reaching a peak. Furthermore, the dispersions undergo a color change to a dark gray during irradiation. A maximum H_2 yield of over 2.3 mmol h^{-1} was achieved at a loading of 5 wt%. These observations suggest that the oxide may undergo a partial reduction, potentially involving the formation of Cu^+. The initial activation is presumed to occur rapidly at low loadings and is therefore not observable. In contrast, at very high loadings, it occurs over the course of the first hours. The elevated activity of TiO_2 P25 with 5 wt% of $CuFe_2O_4$ loaded on top can be attributed to an altered charge transfer mechanism in comparison to solar irradiation, which involves charge excitation in the ferrite as well. Two effects likely contribute to the charge transfer mechanisms and balance best at 5 wt%. On one hand, increased charge excitation at high intensity requires the extraction and conversion of these charge carriers. If utilization of these carriers for the reduction of protons is limited either by mass-transport or kinetics, a higher number of active sites, representing a higher cocatalyst loading can be

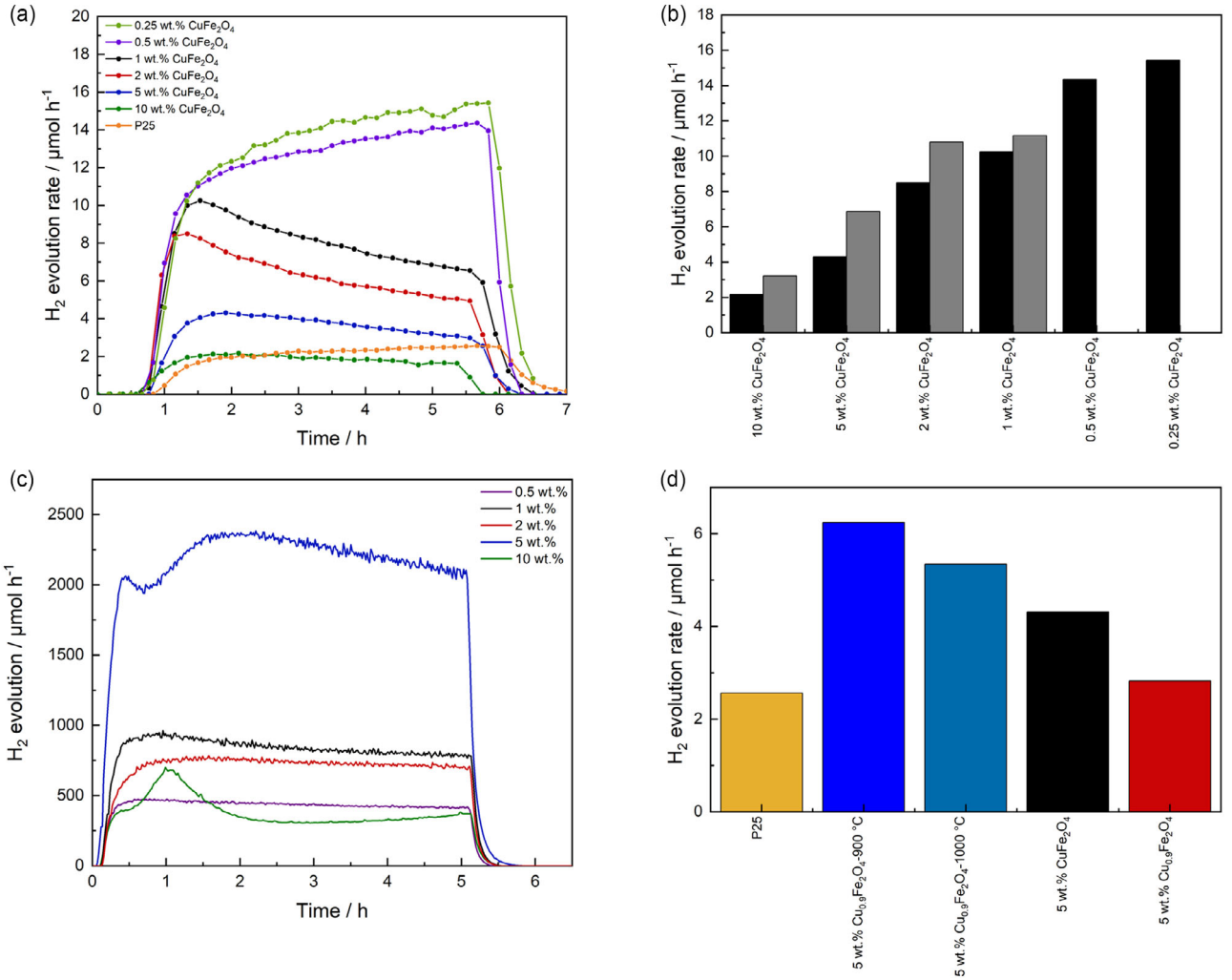

FIGURE 2 | The course of the H_2 evolution over time for different loadings of $CuFe_2O_4$ under simulated sunlight is depicted in (a). Maximum H_2 evolution rates are summarized in (b). They gray columns represent a second 3 h measurement for better comparison with additional cocatalysts in the following. The course of H_2 evolution under intense UV irradiation is depicted in (c), while (d) shows the maximum evolution rates for calcined $CuFe_2O_4$.

beneficial. On the other hand, increased charge excitation in $CuFe_2O_4$ may result in accumulation of electrons in the conduction band of the ferrite, preventing efficient transfer from TiO_2 to the cocatalyst. Kezzim et al. synthesized a composite comprising tetragonal $CuFe_2O_4$ and anatase. They proposed that charge excitation in $CuFe_2O_4$ and subsequent electron transfer to TiO_2—a mechanism that would be expected based on relative band positions, but detrimental to the function of a cocatalyst, as it is opposing the electron flow to the cocatalyst and might become competitive at high loadings—occurred [40–42]. Charge accumulation, trapping, and recombination in $CuFe_2O_4$—partially perhaps due to defects induced by reduction—will then result in an activity loss at high loadings (above 5 wt%). Additional adverse effects, such as shadowing and the intrinsically lower activity and low conductivity of bulk $CuFe_2O_4$, result in a further reduction in performance at higher $CuFe_2O_4$ ratios (10 wt%). Partial reduction of $CuFe_2O_4$ under illumination is additionally supporting the role of the ferrite as a reduction cocatalyst since it indicates electron transfer to the ferrite. The reduction further alters the electronic structure of the ferrite, shifting the d-band center and band positions, and changes material conductivity.

Next, we investigated the impact of annealing on the viability of $CuFe_2O_4$ as a cocatalyst. To prevent Cu segregation, a Cu-deficient stoichiometry $Cu_{0.9}Fe_2O_4$ was selected as the precursor material, which was then annealed at 900°C and 1000°C for 20 h before being quenched in air to room temperature (see previous studies) [35]. The primary distinction between the two samples is the more tetragonal structure observed in the $CuFe_2O_4$ annealed at 900°C, in comparison to the more cubic structure observed in the sample annealed at 1000°C. Subsequently, 5 wt% of the annealed ferrite was loaded onto TiO_2 P25. Upon exposure to solar light irradiation, slightly elevated but analogous H_2 evolution rates were attained (Figures 2d and S4). However, under UV irradiation, the observed activity was markedly lower at the same mass loading (Figure S4). This is likely attributable to the significantly larger particle size of the annealed $CuFe_2O_4$ (with diameters of several hundred nanometers), which impedes the formation of a substantial contact area and may also contribute to the detachment of particles at elevated H_2 production rates. It is noteworthy that the decoration of TiO_2 P25 with 5 wt% of $Cu_{0.9}Fe_2O_4$ yields a comparable H_2 evolution efficiency to that of stoichiometric $CuFe_2O_4$ under UV irradiation. Furthermore,

the activation process appears to proceed over a longer period of time and additionally exhibits two distinct phases. This may be attributed to the larger spatial separation of Cu-centers and the reduced quantity of active Cu-centers.

2.3 | Additional Cu- and Fe-Sulfides

Given the promising results observed with $CuFe_2O_4$ as a cocatalyst for the HER, we proceeded to conduct further studies on the Cu-Fe system with the objective of enhancing its performance. Given that Ni_2FeS_4 had previously demonstrated efficacy as a catalyst for the HER [37], particularly in comparison to the related oxide [14], we proceeded to synthesize CuS, FeS_2, and $CuFeS_2$ via microwave-assisted techniques and evaluate their potential as cocatalysts. The development of these syntheses was adapted from the parameters utilized for $CuFe_2O_4$ and is outlined in Scheme 1. All syntheses employ water or ethylene glycol as low-cost, nontoxic solvents, as well as low-cost, abundant metal salts as precursors. This, in combination with short reaction times and comparatively low required temperatures, enables an economic synthesis of large amounts of these materials.

All Cu-based materials exhibit a nanoparticulate morphology, although the particle size of CuS is slightly larger than that of $CuFeS_2$ and $CuFe_2O_4$ (Figure 3). This is reflected in the larger crystallite size, which is approximated from the powder XRD data via the integral breadth method. The crystallite size for $CuFe_2O_4$ is 6.6 nm, for $CuFeS_2$ it is 6.3 nm, for CuS it is approximately 12 nm, and for FeS_2 it is 25 nm. Therefore, the primary reflection associated with FeS_2 is observable in the XRD patterns of P25 decorated with FeS_2. In contrast, the XRD patterns of composites with 5 wt% of either of the other cocatalysts only exhibit reflections that are characteristic of TiO_2 (Figures 3 and S2).

Similarly, the Raman and IR data (Figure 3) demonstrate the anticipated signals for TiO_2. Additionally, the DRIFT spectra indicate the presence of organic compounds, which may originate from the *i*-propanol utilized in the formation of the composite or from residual organic matter derived from the solvent employed in the synthesis of the Cu- and Fe- sulfides and -oxides. Given the high volatility of *i*-propanol, it is more probable that the latter origin is correct. This is further supported by the observation that the amount of organic compounds is lowest for CuS, which was synthesized in water, and highest for $CoFe_2O_4$, $NiFe_2O_4$, and $CuFeS_2$, all of which were synthesized exclusively in organic solvents.

The resulting composites exhibited a brown/gray hue following the incorporation of transition metal oxides/sulfides, which was accompanied by an elevated diffuse absorption of visible and NIR light (Figures 3 and S2). This phenomenon was particularly pronounced in the case of the black sulfides. In the Kubelka–Munk plots, only the band gap of TiO_2 is discernible. A slight decrease in the band gap is indicated, from 360 to 363 nm, which corresponds to a decrease in energy from 3.6 to 3.4 eV (Table S1). However, this may also be attributed to a partial overlap with the band gaps (and/or locally restricted optical transitions) of the oxides/sulfides, which are reported to be 1.9 eV for $CuFe_2O_4$ [39], approx. 0.6–1.1 eV for $CuFeS_2$ [43, 44], 1.8 eV for CuS [28], and around 1 eV for FeS_2 [45].

The initial methodology for the composite formation entailed an annealing step in air. However, the composites formed with $CuFeS_2$ and FeS_2 exhibited a notable brownish hue at low sulfide loadings, whereas at high loadings, they were of grayish appearance. Given the discrepancy between the observed coloration of the composites and the lack of observable signs of oxidation in the bulk material, we hypothesize that oxidation may have occurred at low loadings due to a larger exposed surface ratio. To address this, we repeated the preparation process with an annealing step in argon instead of air. Indeed, even at low loadings, the obtained composites exhibited a gray coloration rather than the anticipated brown. In accordance with the aforementioned findings, the absorption of visible and near-infrared light is enhanced under these conditions. It is noteworthy that the DRIFT spectra of composites containing $CuFeS_2$ and FeS_2 that were annealed in either argon or air also exhibited discernible differences (Figure S2). In particular, a shoulder present at approximately 1120 cm^{-1} is markedly more prominent in samples that have undergone calcination in air. This is indicative of the formation of sulfate groups [46].

Photocatalytic H_2 evolution was conducted for composites with cocatalyst loadings of 1–10 wt% for 3 h under 1 sun light irradiation (see Figures 4 and S5). It is noteworthy that the various sulfides of the Cu-Fe family exhibited a distinctly disparate behavior from that observed with the oxides discussed earlier. Additionally, notable differences in their H_2 evolution over time were observed between the sulfides. To facilitate comparison, the experiments were repeated for $CuFe_2O_4$ for additional 3 h, and the resulting data are presented as gray bars in Figure 2. While a minimal loading was advantageous for the oxides, a higher loading of 10 wt% is necessary for samples containing FeS_2, despite the darker color (smaller band gap) that should facilitate parasitic light absorption. The highest level

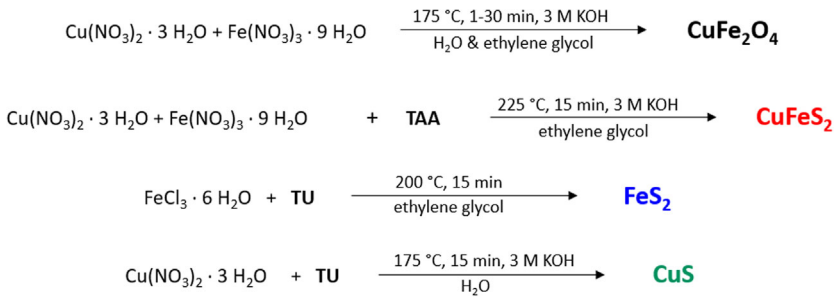

SCHEME 1 | Syntheses of Cu- and Fe-sulfides. TU stands for thiourea, whereas TAA is short for thioacetamide.

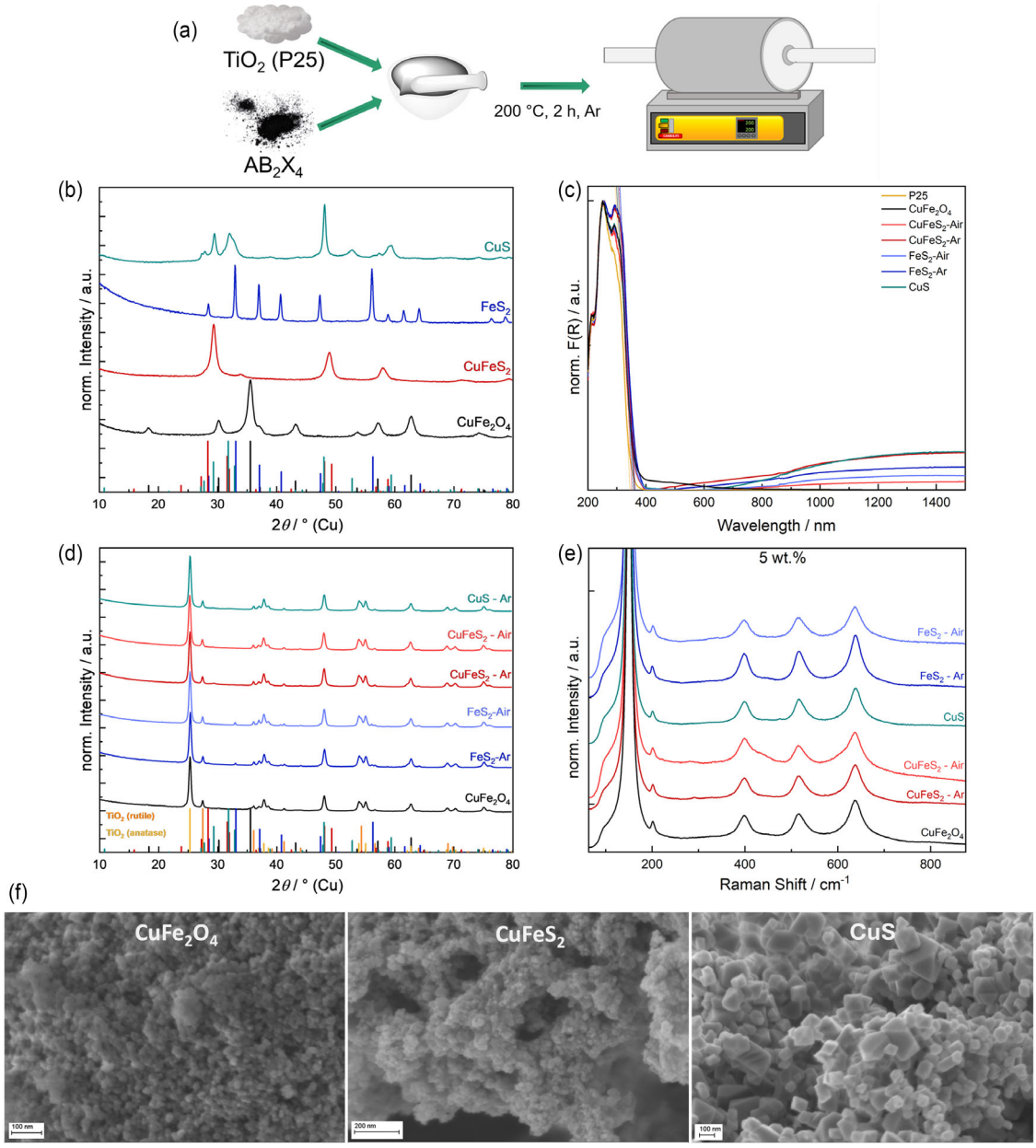

FIGURE 3 | A scheme for the loading of the nanoparticulate cocatalysts onto P25 is shown in (a). (b) shows the XRD patterns for the cocatalyst particles themselves, while (c) depicts the Kubelka–Munk plots for the loaded P25 samples, and (d,e) show the XRD patterns and Raman spectra, respectively. SEM images of Cu-based cocatalysts are depicted in (f).

of activity was achieved with $CuFeS_2$ and CuS at an optimal mass loading of 5 wt%.

Another noteworthy finding is the markedly enhanced activity observed in composites comprising FeS_2 and $CuFeS_2$ when the annealing process was conducted in air as opposed to argon. This indicates that surface oxidation of the sulfide is advantageous and may suggest an oxyhydroxide character as the active species of the cocatalysts under operation. An additional possibility is that the presence of surface sulfate groups can directly enhance the activity. The dissolution of metal sulfates in aqueous media results in the formation of undercoordinated metal sites, which serve as active centers for the reaction, improving the catalytic properties of the cocatalyst [47, 48]. Furthermore, it has been demonstrated that dissolved sulfate groups facilitate oxygen evolution. Consequently, it is plausible that they exert an influence on other reactions, including water reduction and methanol oxidation [49]. In comparison to $CuFe_2O_4$ at a mass loading of 5 wt%, CuS and $CuFeS_2$ annealed in air have been identified as superior cocatalysts under solar light irradiation, with H_2 evolution rates reaching 13.2 and 13.3 $\mu mol\ h^{-1}$, respectively. However, the 5 wt% loading represents the optimal loading for these cocatalysts, and neither cocatalyst can reach the activity observed for $CuFe_2O_4$ at a loading of 0.25 wt%. Given that the activity is increasing for FeS_2 (annealed in air) with an increasing loading, this cocatalyst outperforms the other materials at a loading of 10 wt%, reaching a comparable activity to $CuFe_2O_4$ at 0.25 wt% loading. A mass ratio of 10 wt% is arguably not a common choice for cocatalysts and may suggest the formation of a heterojunction. The higher required mass ratio of CuS compared

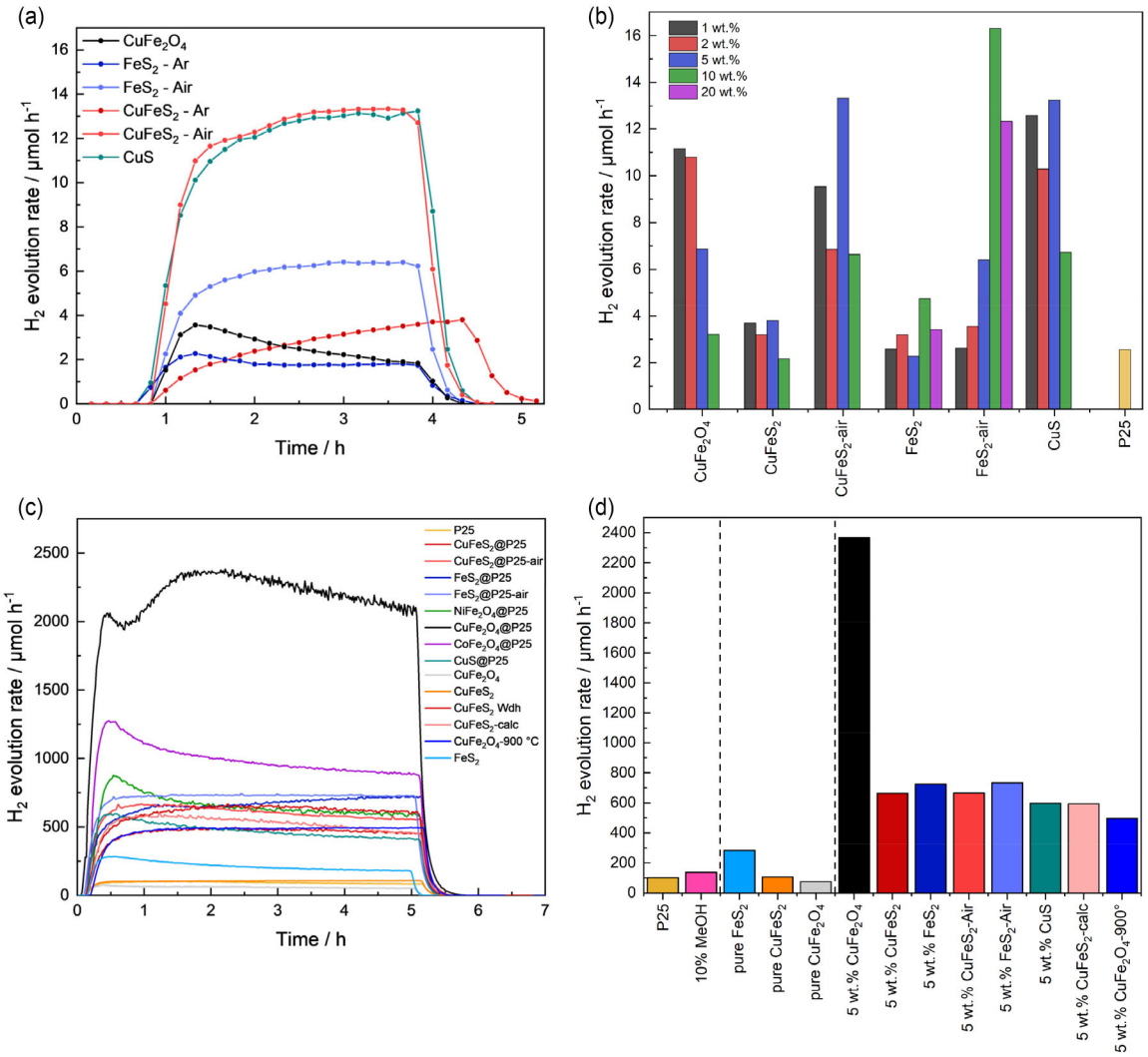

FIGURE 4 | Photocatalytic HER for different Cu- and Fe-based cocatalysts under AM 1.5G simulated sunlight at a loading of 5 wt% (a), and depicted as maximum activity for different loadings (b). H_2 evolution curves under illumination from a 500 W Hg lamp for the different cocatalysts (5 wt%) are depicted in (c), with a summary of maximum activities shown in (d).

to $CuFe_2O_4$, might in parts be due to the larger particle size, which signifies a lower surface area available for the catalytic conversion reaction at the same mass loading, and longer charge transfer pathways through the catalyst. Interfacial contact is probably also worse. Varying synthesis parameters for the preparation of CuS to reduce particle size might therefore enable lower mass loadings.

In addition to the relationship between mass loading and activity, the shape of the H_2 production curves differs between samples. The H_2 evolution rate is highest in the beginning when $CuFe_2O_4$ and FeS_2 are employed as cocatalysts. However, it is quite stable—if slightly increasing—when $CuFeS_2$, CuS, or FeS_2 are subjected to annealing in air and subsequently used as cocatalysts. To some extent, the enhanced stability is associated with the activity, which is reminiscent of the trend observed for $CuFe_2O_4$ employed in different mass loadings.

While the formation of sulfides has been demonstrated to enhance the performance of Cu-Fe cocatalysts, the HER activity achieved with a 5 wt% loading of $CuFe_2O_4$ could not be matched by any of the sulfides under UV light irradiation. Instead, they all exhibit comparable activity within the range of 500–750 µmol h^{-1}. It is noteworthy that with the exception of CuS, there was no initial material activation, but rather a relatively stable performance throughout the duration of the experiment. These findings indicate that the sulfides (or at least the active species) exhibit good stability. However, they also highlight the superior performance of $CuFe_2O_4$ as a cocatalyst. The activity of FeS_2 annealed in air and in argon is identical at the conclusion of the experiment. A gradual increase in activity is observed for FeS_2 annealed in argon, indicating a gradual oxidation of the material. This oxidation process appears to be unrelated to the pronounced activation process observed for $CuFe_2O_4$. Therefore, it can be inferred that the oxidation process is connected to a reduction of Cu rather than Fe. In the case of CuS, the inability to compete at a 5 wt% loading can in parts be explained by the larger particle size, leading to a more pronounced influence of bulk parameters, such as lower conductivity, less active sites, and higher recombination. The physical contact with TiO_2 is assumedly also worse, preventing efficient charge transfer and making it more prone to detachment.

Another readily apparent distinction between the most active cocatalysts, $CuFe_2O_4$ and Ni_2FeS_4, is the absence of Ni, apart from the lack of sulfur. Given that the formation of sulfides did not result in an increase in activity under UV irradiation, it can be concluded that the sulfide/oxide character is not the determining factor for the high activity observed in Cu-cocatalysts. Another notable distinction pertains to the oxidation state of Fe, which is +III in $CuFe_2O_4$ and +II in Ni_2FeS_4. Given that FeS_2 was not any more active than $CuFe_2O_4$, this is unlikely to be a crucial factor. Additionally, the mass ratio of Ni in the sulfide is higher than that of Cu in the oxide. The mass ratio of Cu in CuS should be even higher, although in this specific case, additional factors relating to the higher particle size might have a dominant effect. In addition to the differing characteristics of the metals, the oxidation states also diverge: The oxidation states of copper and nickel are +II with low amounts of +I and +III, respectively. Furthermore, there may be discrepancies in the ease with which Ni^{3+} is partially reduced in comparison to the ease with which Cu^{2+} is reduced. Both should be more readily reduced than Fe^{3+}, which is highly stable due to its d^5 electron configuration. Therefore, in $CuFe_2O_4$, the reduction of Cu^{2+} occurs at more oxidizing potentials than the reduction of Fe^{3+} [50]. Ni^{3+} reduction to Ni^{2+} is usually observed at even more positive potentials in cyclic voltammetry measurements [51].

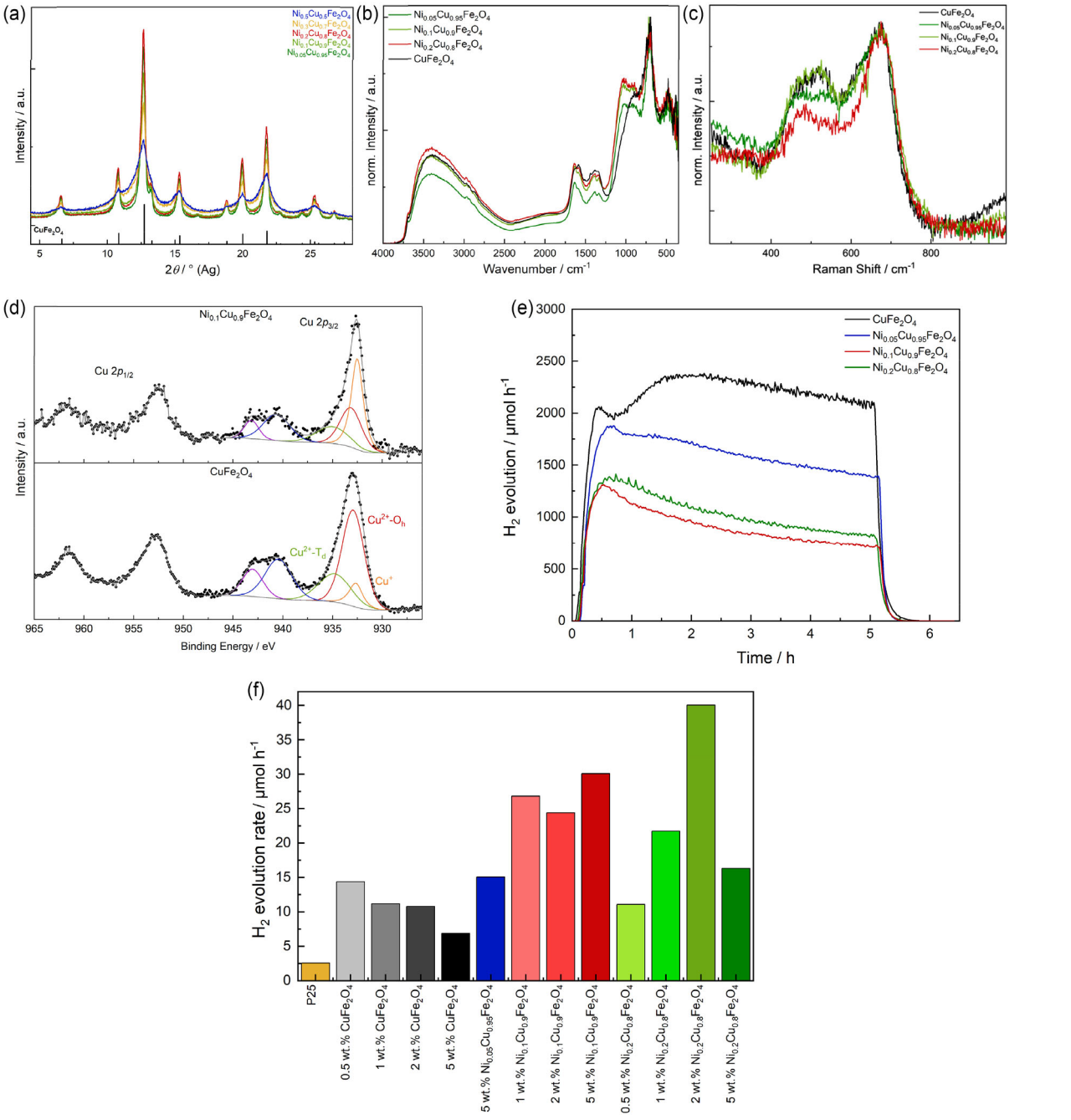

FIGURE 5 | (a) XRD patterns of Ni-doped $CuFe_2O_4$, (b) DRIFT spectra, (c) Raman spectra, (d) Cu 2*p* XP spectra, and (e) photocatalysis results of P25 decorated with the doped $CuFe_2O_4$ under intense UV irradiation, and (f) under simulated sunlight.

2.4 | Ni-Doping of $CuFe_2O_4$

In order to gain further insights into the occurring processes and explore strategies for further increasing the activity of the $CuFe_2O_4$ cocatalyst, a partial substitution of Cu with Ni was conducted. The quantity of Ni-dopant was varied between a molar ratio of 5%–50% (based on the total Ni+Cu), which resulted in a notable loss of crystallinity in the formed $Ni_xCu_{1-x}Fe_2O_4$ samples, accompanied by an increase in the surface area (Figures 5 and S6). The formation of traces of a red precipitate was observed following the centrifugation of synthesis products with Ni concentrations of 30% or higher. This may indicate the formation of metallic Cu or Cu_2O, though neither of these is clearly identifiable in the XRD patterns. Nevertheless, we concentrated on the lower doping amounts to circumvent any potential contributions from unknown impurities. In addition to the reduction in crystallite size, minor variations in the structure are discernible in the DRIFT and Raman spectra (Figure 5). In particular, the broad bands at approximately 500 cm^{-1}, which correspond to T_{2g} vibrations, exhibited a reduction in intensity relative to those at approximately 700 cm^{-1}, which correspond to A_{1g} vibrations [52]. Concurrently, the peak at 500 cm^{-1} for the broad band is diminished on the right side, while a shoulder to the left of the primary peak for A_{1g} vibrations essentially vanishes. These observations strongly indicate alterations in the cation distribution within the spinel structure and a pronounced reduction in the degree of inversion upon doping with Ni [52]. This structural evolution can be rationalized by the fact that Ni is known to prefer an octahedral coordination environment, thus forming an almost entirely inverted structure in $NiFe_2O_4$. In this case, it is possible that Cu is pushed to the tetrahedral sites as a result. Given that both Cu-O and Ni-O vibrations on octahedral (and tetrahedral) sites are expected to occur at slightly different wavenumbers, the relative intensity of the corresponding bands compared to those of Fe-O vibrations necessarily decreases. This results in a similar effect as a transition from a mostly inverse to a normal spinel structure. Therefore, it is not possible to draw any definitive conclusions about changes in the cation environment based on the Raman spectra. To obtain further insight, high-resolution X-ray absorption spectroscopy (XAS) data would be required, which is beyond the scope of this study.

In consideration of the DRIFT spectra, a markedly elevated feature at ~1050 cm^{-1} was discerned, which may be indicative of polyethylene glycol [53]. This, in turn, suggests that Ni facilitates the polymerization of the solvent, which appears to be a reasonable assumption given that Ni-complexes are known oligomerization catalysts for ethylene [54, 55]. Lastly, X-ray photoelectron spectroscopy (XPS) analysis was performed on $Ni_{0.1}Cu_{0.9}Fe_2O_4$, which revealed a significantly increased amount of Cu^+ in the structure compared to $CuFe_2O_4$ (Figures 5, S7, and Table 1). The presence of Cu^+ species indicates the concomitant presence of reduced Fe-species or O-vacancies, which serve to preserve charge neutrality. If the concentrations of both elements were approximately equal in both the stoichiometric $CuFe_2O_4$ and the doped one, a partial replacement of Cu by Ni (which is assumed to be present only as Ni^{2+}) could facilitate the partial reduction of Cu^{2+} to Cu^+. The spectra furthermore indicate an increased fraction of Cu^{2+} in tetrahedral vs. octahedral coordination, which might either be explained by Ni favoring octahedral sites or by Cu+ preferentially occurring in an octahedral coordination environment. Further confirmation of oxidation states and coordination environment—also in operando–would be possible with X-ray absorption spectroscopy. While those mechanistic studies exceed the scope of this work, these results present a good starting point for further investigation in this direction. The calculated (Cu+Ni)/Fe ratio is around the expected ratio of 1/2 (Table S2). The results from DRIFT spectroscopy are in accordance with the observed differences in the organic species adsorbed on the surface. Notably, the presence of Ni resulted in a more pronounced signal corresponding to C—C and C—H bonds.

TABLE 1 | Ratio of respective Cu-species derived from fitting the Cu 2p spectra.

	% Cu^+	% Cu-O_h	% Cu-T_d	λ
$CuFe_2O_4$	11.17	64.81	24.02	0.73
$Ni_{0.1}Cu_{0.9}Fe_2O_4$	46.43	32.78	20.78	0.61

$Ni_xCu_{1-x}Fe_2O_4$ with varying quantities of Ni-dopant were loaded onto TiO_2 P25 and evaluated for their photocatalytic H_2 evolution potential. Initially, a mass loading of 5 wt% was employed (Figure S8). The observed activity exhibited a more than twofold increase even for low nickel ratios of 5% based on the total (Ni + Cu) concentration for experiments conducted under simulated sunlight (Figure 5). The shape of the curves was notably different (Figure S8c). For $Ni_{0.05}Cu_{0.95}Fe_2O_4$, an initial period of high activity is observed, which then declines rapidly. This is similar to what was previously observed for 1 and 2 wt% of $CuFe_2O_4$ on TiO_2. The final activity is also comparable to that of the aforementioned samples. Conversely, when 20% of the Cu was replaced with Ni, a gradual and comparatively minor decline in activity was observed, more akin to that observed with 5 and 10 wt% $CuFe_2O_4$ on TiO_2. At an intermediate Ni concentration of 10%, however, the course of the HER over time is entirely distinct. A two-step activation process was observed, similar to that previously noted for the HER with $CuFe_2O_4$ under UV irradiation. The maximum activity reached was 30 μmol h^{-1}, representing a fourfold increase in activity compared to stoichiometric $CuFe_2O_4$.It can be concluded that a substitution of 10% Cu by Ni is optimal at this loading.

The reduction of the mass loading of $Ni_{0.1}Cu_{0.9}Fe_2O_4$ with the objective of enhancing the activity under solar light irradiation did not yield the desired outcome. The overall HER activity remained largely unchanged across the investigated range of 1–5 wt%, which suggests that the further activation of the material is insignificant in comparison to the material changes already induced by the doping of Ni. The XPS measurements demonstrated that Ni doping increases the relative amount of Cu^+ in the sample. This is particularly advantageous under solar irradiation, as it presents an already activated (partially reduced) form, which is likely the reason for the enhanced activity. Reduced Cu species can, at low concentrations, promote activity, for example by increasing conductivity or offering active sites for the reaction. However, at high concentrations, they act as recombination centers. The observed reduction in activity at 20% Ni substitution is likely attributable to a significant decline in Cu content and a concomitant loss of crystallinity. Furthermore, the already

elevated concentration of Cu^+ can account for the absence of an initial surge in the H_2 evolution curves, as any additional increase is inconsequential. The initially high activity observed at low Ni concentrations, which subsequently declines, is reminiscent of the HER curves for numerous Cu-containing samples under UV irradiation.

In light of the relatively stable curve shape, we proceeded to reduce the mass loading of $Ni_{0.2}Cu_{0.8}Fe_2O_4$, which yielded a further increase in the H_2 evolution rate up to 40 µmol h^{-1}. This is reasonable, given that a reduction in the overall amount of Cu^{2+} will result in an increased relative impact of photoreduction, assuming a similar reduction rate. Consequently, the curve's shape now demonstrates a gradual increase in activity, similar to that observed for very low loadings of $CuFe_2O_4$. This gradual increase may only be observable if the majority of Cu centers are reduced. It is noteworthy that the highest activity is observed at a mass loading of 2 wt%, which differs from the observations made for $CuFe_2O_4$. Subsequently, recombination may be the cause of the reduced activity. The impressive activity obtained with the Ni-doped $CuFe_2O_4$ under simulated sunlight surpasses that of most photocatalytic systems employing Cu- and/or Fe-based cocatalysts (Table S3), and considering the very low overall metal loadings that can be realized, it does not fall far behind Pt applied in comparable amounts [37].

Under UV irradiation, the situation is distinct. When composites containing 5 wt% of the Ni-doped $CuFe_2O_4$ are irradiated by a Hg lamp operated at 500 W, no secondary activation phase is discernible, and the overall activity declines with an increasing Ni concentration (Figure 5). The presence of Cu^+ in the catalyst prior to light irradiation is of lesser importance, as the higher photon flux facilitates photoreduction. In particular, for higher Ni concentrations, charge trapping and recombination are likely to become a significant issue.

Given that Cu^+ is considered the active species for H_2 evolution, it is curious that $CuFeS_2$ exhibits such a marked deficiency in performance relative to $CuFe_2O_4$, given that in this case, all Cu should be in an oxidation state of +I. Furthermore, CuS exhibited minimal activation. It is noteworthy that the crystal structures of $CuFeS_2$ and CuS_2 and, consequently, the coordination environment of Cu and Fe, is markedly distinct from those of the oxides. In $CuFeS_2$, Cu^+ is tetrahedrally coordinated by S, as is Cu^{2+} in CuS [56–58]. Conversely, due to a partial inversion of the spinel structure in $CuFe_2O_4$, the majority of Cu^{2+} is in octahedral coordination [39]. In contrast, the crystal structures of $CuFe_2O_4$ and Ni_2FeS_4 are highly similar—both being spinels, with slight differences in the distribution of Ni/Cu and Fe ions in the lattice and in the lattice parameters. Therefore, it can be posited that the Ni/Cu coordination in an octahedral environment, in conjunction with in situ reduction, is a pivotal factor in the superior activity observed for these two transition metal spinels, which surpass that of compositionally analogous materials. If Ni doping were to displace Cu to the tetrahedral sites and result in a more typical spinel structure, this would further explain the observed decrease in activity for high dopant ratios. XPS data indicate a slight decrease in the degree of inversion (Table S2).

Furthermore, the diminished activity of Cu-deficient ferrite $Cu_{0.9}Fe_2O_4$ in the presence of solar light irradiation and the delayed activation under UV irradiation remain unresolved. The nomenclature of $Cu_{0.9}Fe_2O_4$ is somewhat misleading in that it may imply the existence of Cu vacancies. Nevertheless, the ratio of copper in the preparation of $Cu_{0.9}Fe_2O_4$ is merely diminished. Given that a spinel can still be formed and redox reactions may occur under the conditions employed, it is more accurate to consider the formed product to be Fe-rich rather than Cu-deficient. Given that copper typically exhibits a lower oxidation state than iron (+2 instead of +3), the structure of Fe-rich $CuFe_2O_4$ can undergo charge compensation via three primary pathways: (1) oxygen deficiency; (2) partial reduction of Fe; and (3) a decreased average oxidation state of Cu (if Cu^{2+} ions are replaced by Fe^{3+} ions). Indeed, a higher concentration of Cu^+ is observed by XPS, which should, in principle, enhance the performance. The absence of this effect may be indicative of the involvement of multiple Cu centers in the conversion mechanism.

Future work will focus on further elucidating the effect of Ni-doping on the electronic structure of $CuFe_2O_4$. Especially XAS would be a powerful tool in revealing the valence states of Cu, Fe, and Ni present in the material in addition to elucidating the local coordination environment. While those studies exceed the scope of this work, transition metal doping of $CuFe_2O_4$ has proven a promising strategy for tuning the activity of transition-metal cocatalysts and opens an interesting avenue for future work on the topic. Especially for a medium loading of 5 wt% of $CuFe_2O_4$ on TiO_2, *operando* XAS studies could provide insights

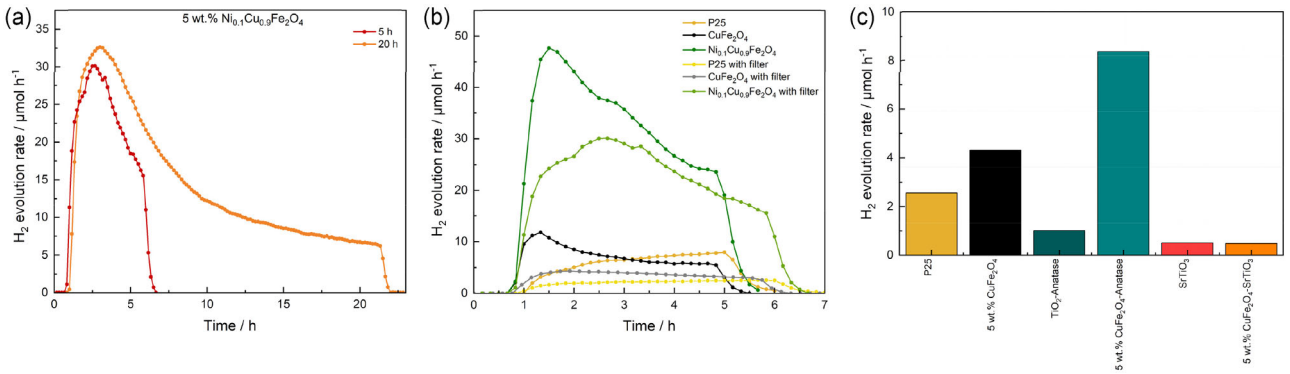

FIGURE 6 | (a) 20 h experiment with 5 wt% $Ni_{0.1}Cu_{0.9}Fe_2O_4$ under simulated sunlight and (b,c) H_2 evolution with additional photocatalysts loaded with 5 wt% of $CuFe_2O_4$.

into partial material reduction. Coupled to techniques such as transient absorption spectroscopy (TAS), such investigations may unravel charge transfer mechanisms in the system and represent strategies we aim at pursuing in the future. Additionally, an improvement of the cocatalyst loading onto TiO_2 using alternative methods offers the potential to further increase the efficiency of the $CuFe_2O_4$ cocatalyst by preventing particle agglomeration, increasing the number of accessible sites, reducing recombination at particle–particle interfaces, and reducing charge transfer pathways further. This might result in further activity increase and lower loadings achieveable.

2.5 | Affirming the Suitability of $CuFe_2O_4$ as an Earth-Abundant Cocatalyst

To further substantiate the suitability of $CuFe_2O_4$ and Ni-doped $CuFe_2O_4$ as cocatalysts for photocatalytic HER, additional experiments were conducted. Initially, a long-term test was conducted over a 20 h period for a 5 wt% solution of $Ni_{0.1}Cu_{0.9}Fe_2O_4$ (Figure 6). It is regrettable to note that, as was indicated in the measurement conducted over a period of 5 h, the activity of the material in question declines significantly with the passage of time. This decline is gradual and culminates in a value that is comparable to that observed for $CuFe_2O_4$. This suggests that either there is a loss of Ni or that there is an increase in the number of defects and recombination events.

Moreover, we conducted an experiment in which we tested $CuFe_2O_4$ and $Ni_{0.1}Cu_{0.9}Fe_2O_4$ under irradiation with a 150 W Xe lamp without the sun filter. The intensity of visible light was thus comparable to that of previous experiments, while the UV irradiation was increased. Additionally, high-intensity spikes appeared at wavelengths greater than 800 nm [59]. It is anticipated that the elevated UV light intensity will lead to an increase in activity, given that a greater number of photons will be absorbed by the photocatalyst, TiO_2. Indeed, the observed H_2 evolution rate was more than doubled for pristine TiO_2 P25 in comparison to measurements with an AM 1.5G filter (Figure 6b). The observed increase in activity is less pronounced for the same material decorated with $Ni_xCu_{1-x}Fe_2O_4$ catalysts, which is likely due to the lower amount of photocatalyst and additional shadowing effects. It is noteworthy that the initial activity spike is far more pronounced under these conditions, which is in accordance with the larger amount of absorbed photons that promote Cu reduction.

Finally, we synthesized composites with $CuFe_2O_4$ in combination with various photocatalysts to demonstrate the universal applicability of this approach (Figure 6c). The utilization of anatase as a photocatalyst results in a considerably more pronounced enhancement in activity. Pristine anatase exhibits lower activity than TiO_2 P25, which can be attributed to the absence of a heterojunction that could assist in charge separation. Conversely, this suggests that electron transfer predominantly occurs from anatase to $CuFe_2O_4$, which is reasonable given that electron transfer from rutile to anatase is also assumed for TiO_2 P25 [60]. $SrTiO_3$ has practically no activity under solar light irradiation—consequently, the addition of a $CuFe_2O_4$ cocatalyst did not have an effect, since electron extraction cannot be promoted, if they are not generated in the first place.

Cocatalysts utilized to facilitate charge extraction and conversion in a photocatalytic reaction are, in essence, electrocatalysts. Consequently, electrochemical HER was also measured for the employed cocatalyst materials in both 1 M KOH and 0.5 M H_2SO_4 (Figure S10). In general, the pH during photocatalysis is maintained at a neutral level. However, localized fluctuations in pH are anticipated. Given that the HER is consuming protons, it is more probable that a locally increased pH will occur. However, the oxidation of water and methanol can produce protons, and the spatial separation of oxidation and reduction sites is minimal in photocatalysis. In the presence of base, FeS_2 exhibits the highest activity as a HER catalyst, followed by $CuFeS_2$ and $CuFe_2O_4$. This suggests that Fe-centers are indispensable for the reaction. This performance trend is analogous to that observed under solar irradiation with the partially oxidized sulfides. Given the alkaline environment's high oxidative capacity, partial oxidation of the sulfide catalysts is a reasonable assumption. In contrast, under acidic conditions, only CuS and $CuFe_2O_4$ demonstrated sustained activity after 20 cycles, suggesting the potential for material degradation, particularly in the case of the Fe-containing samples. It is noteworthy that both the bias and the current densities are significantly higher in electro- compared to photocatalysis. In addition, a correlation with photocatalysis under irradiation from the Hg lamp (higher photon flux) is more probable than one using simulated sunlight. The discrepancy in observations can be attributed to the differing durations of the experiments. While the photocatalytic experiment is conducted over the course of several hours, maintaining constant reducing conditions at the cocatalyst, the LSV scans are performed in a much shorter time frame. Between sweeps, the potential is returned to values just above 0, which can be slightly oxidative, particularly in an alkaline environment. This may prevent extensive material reduction. Prior research on $CuFe_2O_4$ has demonstrated that the activity of the material increases significantly when a reducing potential is maintained for an extended period of time [34]. Furthermore, the potential impact of charge excitation in the cocatalyst and the formation of a heterojunction have been excluded from the comparison with electrochemical data. When considering only FeS_2, $CuFeS_2$, and CuS, all of which demonstrate a predominantly stable H_2 evolution over the course of the experiment, the activity trend $FeS_2 > CuFeS_2 > CuS$ is confirmed. Nevertheless, the comparability of the photo- and electrocatalytic measurements remains constrained, and the activity of the aforementioned three catalysts is markedly analogous.

Additionally, electrochemical HER experiments were conducted in 1 M KOH for the Ni-doped $CuFe_2O_4$ to ascertain whether the observed trends in the photocatalytic application could be replicated at elevated bias and current flow. In accordance with the diminished HER activity observed with Ni-doped $CuFe_2O_4$ cocatalysts under UV irradiation, a Ni concentration of 10% or higher has been shown to result in a reduction in the electrochemical HER, thereby further substantiating the deleterious effects of defects (Figure S10). Furthermore, EIS data indicate that lower amounts of Ni dopant initially enhance conductivity, likely due to the higher concentration of reduced Cu-species. However, at high Ni-concentration, the charge transfer resistance increases, likely due to the lower crystallinity and elevated defect concentration (Figure S10). In contrast, the addition of a relatively low amount of Ni-dopant (5%) resulted in a slight enhancement of the observed activity.

2.6 | Post-Catalytic Characterization

In order to investigate the stability of earth-abundant cocatalysts, we employed XRD, IR, and Raman spectroscopy following photocatalysis (see Figures S11 and S12). The majority of reflections and bands are attributable to the TiO_2 photocatalyst. Nevertheless, reflections corresponding to FeS_2 can still be discerned, thereby corroborating the stability of the sulfide cocatalysts. No formation of secondary phases or degradation products was observed, with the exception of signals corresponding to organic degradation products of methanol. To gain further insight into the material changes, we conducted a comparative analysis of TiO_2 P25 loaded with 5 and 10 wt% $CuFe_2O_4$ before and after photocatalysis under irradiation from a 500 W Hg lamp or a solar simulator, respectively (Figure S13). The intensity of the reflections for $CuFe_2O_4$ exhibits only a slight decrease following the experiment conducted under simulated sunlight. Conversely, the reflections almost entirely disappear following the experiment conducted under UV irradiation. This phenomenon can be attributed to a combination of two factors: the detachment of cocatalysts due to the intensified formation of bubbles, or the partial reduction of the material, which ultimately leads to a loss of crystallinity. Cu- and Fe-leaching, as has been observed for Cu-containing photocatalysts (especially sulfide, for which concomitant sulfide oxidation was found), may contribute to the apparent amorphization [61]. In addition, the light absorption in the visible light range is markedly diminished, as evidenced by the composite catalyst's notable pallor (with a yellowish hue). It is noteworthy that an apparent decrease in the band gap of TiO_2 P25 is observed, due to the absorption feature at 304 nm increasing in favor of that at 252 nm. This may be indicative of the formation of defects, such as oxygen vacancies, and thus partial reduction/electron enrichment of the TiO_2 photocatalyst [62]. Cu-single atom cocatalysts on TiO_2 have been shown to promote lattice distortions in TiO_2 due to electric fields being generated by trapped electrons in the Cu *d*-orbitals [63]. A similar effect could be observed in our studies, in agreement to proposed partial reduction of the Cu-catalyst under operation. The reduction may occur either during photocatalysis, if the electrons are not efficiently transferred to the cocatalyst and subsequently to protons, be directly induced by the reduced Cu-species, or it may occur subsequently, concomitant to the re-oxidation of reduced copper species.

3 | Conclusion

A systematic investigation was conducted to ascertain the potential of Cu- and Fe-based oxides and sulfides as earth-abundant cocatalysts for the photocatalytic H_2 evolution reaction over TiO_2 P25. While all the materials were found to enhance the H_2 yield under both simulated sunlight and UV light, $CuFe_2O_4$ exhibited particularly promising behavior. Further investigation revealed that the catalytic properties are significantly influenced by the material loading and irradiation conditions, due to an in situ activation process that is correlated with Cu reduction. At a loading of 5 wt%, a H_2 evolution rate of >2.3 mmol h^{-1} was achieved under irradiation from a Hg lamp operated at 500 W. To enhance the performance under AM 1.5G simulated sunlight, Ni doping was found to be an effective strategy, as it led to a decrease in the average valence of Cu. This strategy resulted in an increase in the H_2 evolution rate to 40 µmol h^{-1}, representing a 15-fold enhancement in activity compared to the bare TiO_2 P25. In conclusion, these results demonstrate the potential of Cu-Fe-based cocatalysts to replace noble metal cocatalysts and illustrate how material engineering can be employed to modify the properties of these cocatalysts for optimal performance enhancement. Of particular significance are the coordination environment and oxidation state of the elements at the active site, which have to be further explored in future studies using XAS. Compared to traditional noble-metal cocatalysts, such as Pt, the costs for Fe- and Cu-precursor salts are substantially lower and the availability considerably higher. In addition to low metal loadings (notably, even 5 wt% of $CuFe_2O_4$ only equal to 1.3 wt% of Cu, with even lower Cu amounts required at lower cocatalyst loadings optimal under 1 sun illumination), and short synthesis times at low reaction temperatures in abundant and nontoxic solvents, offers the potential for economic large-scale fabrication and application.

4 | Experimental Section

4.1 | Synthesis

$NiFe_2O_4$ and $CoFe_2O_4$ were synthesized *via* a nonaqueous microwave-assisted approach as previously reported [33, 38]. 0.5 mmol of M $(acac)_2$ (M = Ni, Co) and 1 mmol of Fe $(acac)_3$ (Acros Organics) were dispersed in 15 mL of rac 1-phenylethanol (Sigma–Aldrich) using ultrasonication for approx. 30 min. The solution was transferred to a 15 mL borosilicate microwave vessel equipped with a stirring bar and heated up as fast as possible to 200°C in a microwave reactor (Anton Paar, Monowave 400). After 30 min at the target temperature, the mixture was cooled down with compressed air. The product was precipitated in n-pentane and washed thrice with acetone/water (30:5) and once with diethyl ether, before being dried over night at 80°C.

The synthesis of $CuFe_2O_4$ was performed according to previous reports [39]. In brief, 1 mmol of $Fe(NO_3)_3 \cdot 9\ H_2O$ (404 mg, 2 eq., Acros Organics) and 0.5 mmol of $Cu(NO_3)_2 \cdot 3\ H_2O$ (120.8 mg, 1 eq., ABCR) were dissolved in a mixture of ultrapure water and ethylene glycol (Acros Organics) in a ratio of 2:1. Directly before the synthesis, 1.6 mL of a 3 M KOH solution were added under stirring to reach a pH of 12. The total liquid volume was 15 mL. The dispersion was heated as fast as possible and under stirring at 800 rpm to a target temperature of 175°C in a microwave reactor (Anton Paar, Monowave 400). After 15 min at 175°C, the mixture was cooled down with compressed air. The product was precipitated, washed thrice with water, once with ethanol, and dried over night at 80°C in air. For the preparation of Ni-doped $CuFe_2O_4$, parts of the $Cu(NO_3)_2 \cdot 3\ H_2O$ were replaced by $Ni(NO_3)_2 \cdot 6\ H_2O$ (ABCR).

For the synthesis of $CuFeS_2$, 0.5 mmol $Fe(NO_3)_3 \cdot 9\ H_2O$ (202 mg, 1 eq., Acros Organics) and 0.5 mmol of $Cu(NO_3)_2 \cdot 3\ H_2O$ (120.8 mg, 1 eq., ABCR) were dissolved in 10 mL of ethylene glycol. Meanwhile, 4 mmol of thioacetamide (TAA, 300.5 mg, 4 eq., Carl Roth) were dissolve in 5 mL of ethylene glycol. Directly before the synthesis, the thioacetamide solution was added under stirring to the metal precursor solution, followed by the addition of 1.6 mL 3 M KOH. The vial (borosilicate glass) was sealed immediately and placed in the microwave reactor (Anton Paar, Monowave 400), where it

was heated as fast as possible to 225°C under stirring at 800 rpm. The reaction mixture was kept at the target temperature for 15 min, before rapidly being cooled down by compressed air. The product was precipitated with ethanol, washed twice with ethanol, once with ethanol-water mixtures in a ratio of 2:1, once in an ethanol water mixture in a ratio of 1:1, and once with diethylether, before being dried over night at 80°C.

0.5 mmol of $Cu(NO_3)_2 \cdot 3\ H_2O$ (120.8 mg, 1 eq., ABCR) were dissolved in ultrapure water for the synthesis of CuS. 3 mmol of thiourea (TU, 228.36 mg, 6 eq., Carl Roth) were added to the solution, followed by 1.6 mL of a 3 M KOH solution. The solution was heated up as fast as possible under stirring to a target temperature of 175°C. After 15 min, it was cooled down rapidly with compressed air. The formed black product was precipitated with ethanol, washed once with an ethanol/ water mixture of 1:1, once with an ethanol/water mixture of 2:1, and once with diethylether, before being dried over night at 80°C.

For the synthesis of FeS_2, 1 mmol of $FeCl_3 \cdot 6\ H_2O$ (270.3 mg, Grüsser) was dissolved in 10 mL of ethylene glycol and transferred to a microwave vessel. 1 mmol of thiourea (TU, 76.12 mg, Carl Roth) was dissolved in 5 mL of ethylene glycol. Directly before placing the vial in the microwave reactor, the solution of TU was added under stirring to the solution of $FeCl_3$. The solution was heated up to 200°C where it was held for 15 min, before cooling down to 55°C with compressed air. The black product was precipitated with ethanol, washed thrice with an ethanol/ water mixture of 2:1, and once with diethylether, before being dried over night at 80°C.

For the preparation of composites with TiO_2 (P25, Aeroxide, Evonik Industries AG), the oxide/ sulfide and TiO_2 were physically mixed in the desired weight ratio and ground together for 10 min in a mortar with the addition of ~1 mL of *i*-propanol. The composite material was subsequently annealed either in air (Nabertherm furnace) or in an Ar atmosphere (Carbolite tube furnace) for 2 hr at 200°C to improve interfacial contact.

4.2 | Characterization

XRD measurements of powders using Cu Kα irradiation, were conducted either on a Malvern PANalytical Empyrean device at an acceleration voltage of 40 V, an emission current of 40 mA, and using a spinning sample holder in Bragg–Brentano geometry, or on a Rigaku SmartLab diffractometer equipped with a rotating copper anode at 200 mA and 45 kV. For measurements with Ag Kα irradiation, a STOE STADI P Mythen2 4 K diffractometer, equipped with a Ge (111) monochromator and four Dectris MYTHEN2 R 1 K strip detectors, was used [64]. The measurements were conducted in transmission geometry using Hilgenberg capillaries with an outer diameter of 0.5 mm. X'pert HighScore plus was used for the identification of crystal phases. The following reference patterns were used: Anatase—ICDD 00-021−1272, Rutile—ICCD 00-021−1276, $CuFe_2O_4$—ICDD 01-077−0010, $CuFeS_2$—ICDD 00-034−1409, CuS—ICDD 01-079−2321, and FeS_2—ICDD 00-042−1340. Crystallite sizes were estimated using the integral breadth method, i.e., dividing the height of a reflection by its area in a plot versus. the scattering vector.

XPS measurements were conducted on a PHI VersaProbe III instrument with Al Kα irradiation. The beam voltage was set to 15 kV, while a power of 25 W and a beam diameter of 100 µm were used. The step size was 0.4 eV with a time per step of 50 ms and a pass energy of 224 eV for survey spectra and 0.1 eV, 50 ms and 26 eV for high-resolution spectra. To prevent sample charging, the samples were continuously flooded with electrons and Ar^+ at low energy. Data evaluation was done with CASA XPS, using a Shirley Back-ground and Gaussian–Lorentzian functions for peak shape modeling (GL30). For charge correction, the K $2p_{3/2}$ peaks were used, due to pronounced differences in the organic species and set to a binding energy of 292.8 eV. The Cu $2p_{3/2}$ and Fe 3*p* peaks were used for elemental quantification.

Scanning electron microscopy (SEM) was performed on a Zeiss Leo 1530 device at an acceleration voltage of 3 kV after Pt sputtering (Cressington Sputter Coater 208 HR). For Raman spectroscopy, a Horiba Yvon Raman microscope was used in combination with a He-Ne laser with a wavelength of 633 nm operated at a power of 11.5 W. The laser intensity was reduced to avoid extensive sample heating and potential decomposition. Spectra were manually despiked. DRIFT spectra were recorded on a Bruker Alpha II spectrometer. UV/vis/NIR spectra were measured on a PerkinElmer Lambda 750 spectrometer equipped with a Praying Mantis (Harrick). Spectralon was used as white standard. The Kubelka–Munk function was used for the calculation of pseudo- absorption, F (R).

For N_2 *physisorption* measurements, a Quadrasorb Evo device (Anton Paar QuantaTec) was used. Samples were degassed for 12 hr at 120°C prior to the measurements, which were conducted at 77 K. Surface areas were determined using the Brunauer–Emmet–Teller (BET) model and the software ASiQwin.

4.3 | Photocatalysis

For the photocatalytic experiments under simulated sunlight, 50 mg of the catalyst were dispersed in ~20 mL of ultrapure water using ultrasonication for 10 min. The dispersion was transferred to a glass reactor equipped with a stirring bar and diluted with water and methanol to a total volume of 150 mL and a total methanol concentration of 10 vol%. The reactor was sealed and flushed for 20 min with Ar at a flow rate of 100 mL min^{-1}. Subsequently, the argon flow was reduced to 25 mL min^{-1} (constant gas flow), and the dispersion was illuminated by a solar simulator (Newport) using a 150 W Xe lamp and a AM 1.5G filter for 3/5 h at 20°C. The produced gasses were continuously measured by gas chromatography (Shimadzu GC-2014).

For measurements under intense UV irradiation, 150 mg of the catalyst were dispersed in ~20 mL of ultrapure water using ultrasonication for 10 min, before being transferred to a home-made glass reactor. The dispersion was diluted with water and methanol to a total volume of 600 mL and a methanol concentration of 10 vol%. The reactor was flushed with argon for min 1.5 h at a flow rate of 100 mL min^{-1}, until the air was removed. Subsequently, illumination was turned on and maintained for 5 h. For this, a 700 W Hg lamp (Peschl Ultraviolet) was used, operated at 500 W. The dispersion was continuously stirred at 250 rpm, cooled to 10°C, and purged with argon at a flow rate

of 100 mL min^{-1}. Evolving gases were monitored using mass spectrometry (HPR-20 Q/C, Hiden Analytical).

4.4 | Electrocatalysis

The electrochemical measurements were conducted in a two-compartment glass cell separated by either a Nafion membrane or a Selemion membrane (AGC group). The cell was continuously purged with Ar. A standard three-electrode system was used, with Pt as the counter electrode and a RHE reference electrode (Hydroflex, Gaskatel). For the working electrode preparation, 10 mg of the catalyst were dispersed in 600 µL of isopropanol and 20 µL of a 5 wt% Nafion solution. Two times 30 µL of the ink were dropcast onto a carbon paper stripe electrode (Freudenberg H2315-C2) with an exposed area of 1 cm^2 restricted by Kapton tape. The measurements were conducted in either 1 M KOH or 0.5 M H_2SO_4. A Gamry potentiostat was used. For measurements in 1 M KOH, a typical measurement sequence consisted of 3 CV cycles, followed by EIS at OCV and at −0.6 V, and finally 25 linear sweep voltammetry scans. For measurements in H_2SO_4, a similar sequence was used, only with a conditioning step before the 20 LSV measurements, consisting of 100 CV cycles from 2 to −0.7 V at a scan rate of 250 mV s^{-1}. For measurements of Ni-doped $CuFe_2O_4$, a similar conditioning step with a scan rate of 1000 mV s^{-1} was employed.

Acknowledgments

The authors thank Lion Schumacher for the XPS measurements, as well as Jonas Jungmann and Dr. Jana Timm for physisorption measurements. Additionally, we thank Dr. Anja Hofmann for the SEM images. The authors gratefully acknowledge the Bavarian Polymer Institute (BPI) for usage of the XPS and SEM instruments in the KeyLabs "Device Engineering" and "Electron and Optical Microscopy". We would further like to thank Jan N. Hetzel for his assistance in the development of a microwave-assisted synthesis of $CuFeS_2$ and CuS, as well as Ole Schröder for his assistance in the lab in the preparation of Ni-doped $CuFe_2O_4$. J.Z. and R.M. are grateful for funding in the graduate school of the Bavarian Center for Battery Technology (BayBatt), University of Bayreuth.

Open Access funding enabled and organized by Projekt DEAL.

Conflicts of Interest

The authors declare no conflicts of interest.

Data Availability Statement

The data that support the findings of this study are available from the corresponding author upon reasonable request.

References

1. D. Tonelli, L. Rosa, P. Gabrielli, K. Caldeira, A. Parente, and F. Contino, *Nature Communications* 14 (2023): 1–14.

2. S. Shiva Kumar and H. Lim, *Energy Reports* 8 (2022): 13793–13813.

3. J. Yang, D. Wang, H. Han, and C. A. N. Li, *Accounts of Chemical Research* 46 (2013): 1900–1909.

4. K. Takanabe, *ACS Catalysis* 7 (2017): 8006–8022.

5. M. S. Faber and S. Jin, *Energy & Environmental Science* 7 (2014): 3519–3542.

6. A. Li, Y. Sun, T. Yao, and H. Han, *Chemistry - A European Journal* 24 (2018): 18334–18355.

7. B. M. Hunter, H. B. Gray, and A. M. Müller, *Chemical Reviews* 116 (2016): 14120–14136.

8. P. Acharya, R. H. Manso, A. S. Hoffman, et al., *ACS Catalysis* 12 (2022): 1992–2008.

9. M. S. Burke, L. J. Enman, A. S. Batchellor, S. Zou, and S. W. Boettcher, *Chemistry of Materials* 27 (2015): 7549–7558.

10. W. Ou, X. Ye, and Y. Zhou, *Coordination Chemistry Reviews* 493 (2023): 215274.

11. M. S. Faber, M. A. Lukowski, Q. Ding, N. S. Kaiser, and S. Jin, *Journal of Physical Chemistry C* 118 (2014): 21347–21356.

12. Q. Han, Y. Luo, G. Liu, Y. Wang, J. Li, and Z. Chen, *Journal of Catalysis* 413 (2022): 425–433.

13. W. Xiong, Z. Guo, H. Li, R. Zhao, and X. Wang, *ACS Energy Letters* 2 (2017): 2778–2785.

14. M. B. Z. Hegazy, J. Zander, M. Weiss, et al., *Small* 20 (2024): 2311627, https://doi.org/10.1002/smll.202311627.

15. L. Tan, J. Yu, C. Wang, et al., *Advanced Functional Materials* 32 (2022): 2200951, https://doi.org/10.1002/adfm.202200951.

16. R. Chen, Z. Zhang, Z. Wang, et al., *ACS Catalysis* 12 (2022): 13234–13246.

17. J. Ran, J. Zhang, J. Yu, M. Jaroniec, and S. Z. Qiao, *Chemical Society Reviews* 43 (2014): 7787–7812.

18. J. Ma, S. H. Ahn, and S. Y. Kim, *Journal of Energy Chemistry* 88 (2024): 336–355.

19. D. Li, J. Shi, and C. Li, *Small* 14 (2018): 1–22.

20. P. Ayala, A. Giesriegl, S. P. Nandan, S. N. Myakala, P. Wobrauschek, and A. Cherevan, *Catalysts* 11 (2021): 417.

21. B. Tudu, N. Nalajala, K. Prabhakar Reddy, P. Saikia, and C. S. Gopinath, *ACS Sustainable Chemistry and Engineering* 9 (2021): 13915–13925.

22. J. Zhang, T. Wang, P. Liu, et al., *Nature Communications* 8 (2017): 1–8.

23. J. Ran, J. Zhang, J. Yu, and S. Z. Qiao, *ChemSusChem* 7 (2014): 3426–3434.

24. Y. Zhong, J. Yuan, J. Wen, et al., *Dalton Transactions* 44 (2015): 18260–18269.

25. Q. Jia, C. Yu, W. Liu, et al., *Journal of Energy Chemistry* 30 (2019): 101–107.

26. Q. Wang, G. Yun, Y. Bai, et al., *International Journal of Hydrogen Energy* 39 (2014): 13421–13428.

27. T. R. Kuo, H. J. Liao, Y. T. Chen, et al., *Green Chemistry* 20 (2018): 1640–1647.

28. A. M. Huerta-Flores, L. M. Torres-Martínez, E. Moctezuma, A. P. Singh, and B. Wickman, *Journal of Materials Science: Materials in Electronics* 29 (2018): 11613–11626.

29. T. R. Hellstern, J. D. Benck, J. Kibsgaard, C. Hahn, and T. F. Jaramillo, *Advanced Energy Materials* 6 (2016): 1501758.

30. D. Zhao, B. Sun, X. Li, L. Qin, S. Kang, and D. Wang, *RSC Advances* 6 (2016): 33120–33125.

31. L. A. King, M. A. Hubert, C. Capuano, et al., *Nature Nanotechnology* 14 (2019): 1071, https://doi.org/10.1038/s41565-019-0550-7.

32. Q. Zhao, Z. Yan, C. Chen, and J. Chen, *Chemical Reviews* 117 (2017): 10121–10211.

33. C. Simon, M. B. Zakaria, H. Kurz, et al., *Chemistry - A European Journal* 27 (2021): 16990–17001.

34. J. Zander, M. F. Fink, M. Attia, C. Roth, and R. Marschall, *Sustainable Energy Fuels* 8 (2024): 4848–4863.

35. J. Zander, F. Daumann, R. Loukrakpam, C. Roth, B. Weber, and R. Marschall, *Advanced Energy and Sustainability Research* 6 (2024): 2400281, https://doi.org/10.1002/aesr.202400281.

36. Y. Y. Sun, X. Y. Zhang, J. Tang, et al., *Small* 19 (2023): 2207965, https://doi.org/10.1002/smll.202207965.

37. J. Zander and R. Marschall, *Journal of Materials Chemistry A* 11 (2023): 17066–17078.

38. J. Zander, J. P. Wölfel, M. Weiss, et al., *Advanced Functional Materials* 2310179 (2023): 1–16.

39. J. Zander, M. Weiss, and R. Marschall, *Advanced Energy and Sustainability Research* 4 (2023): 2200184.

40. A. Kezzim, N. Nasrallah, A. Abdi, and M. Trari, *Energy Conversion and Management* 52 (2011): 2800–2806.

41. J. ichi Fujisawa, T. Eda, and M. Hanaya, *Chemical Physics Letters* 685 (2017): 23–26.

42. S. Park, J. H. Baek, L. Zhang, et al., *ACS Sustainable Chemistry and Engineering* 7 (2019): 5867–5874.

43. M. Fujisawa, S. Suga, T. Mizokawa, A. Fujimori, and K. Sato, *Physical Review* 49 (1994): 7155–7164.

44. Y. Wu, B. Zhou, C. Yang, S. Liao, W. H. Zhang, and C. Li, *Chemical Communications* 52 (2016): 11488–11491.

45. H. Qin, J. Jia, L. Lin, H. Ni, M. Wang, and L. Meng, *Materials Science and Engineering: B* 236-237 (2018): 104–124.

46. M. Maneva, D. Rizova, and L. Genov, *Spectroscopy Letters* 25 (1992): 603–615.

47. C. Karakaya, N. Solati, U. Savacı, et al., *ACS Catalysis* 10 (2020): 15114–15122.

48. Z. Yu, Y. Li, V. Martin-Diaconescu, et al., *Advanced Functional Materials* 32 (2022): 2206138.

49. Y. Shi, W. Du, W. Zhou, et al., *Angewandte Chemie International Edition* 59 (2020): 22470–22474.

50. M. Einert, A. Waheed, D. C. Moritz, et al., *Chemistry - A European Journal* 29 (2023): e202300277, https://doi.org/10.1002/chem.202300277.

51. Y. J. Son, S. Kim, V. Leung, et al., *ACS Catalysis* 12 (2022): 10384–10399.

52. K. R. Sanchez-Lievanos, J. L. Stair, and K. E. Knowles, *Inorganic Chemistry* 60 (2021): 4291–4305.

53. M. T. Caccamo and S. Magazù, *Applied Spectroscopy* 71 (2017): 401–409.

54. F. Speiser, P. Braunstein, and L. Saussine, *Accounts of Chemical Research* 38 (2005): 784–793.

55. C. Chen, *Nature Reviews Chemistry* 2 (2018): 6–14.

56. D. P. R. Moreira, *Inorganic Chemistry* 54 (2015): 4840–4849.

57. M. Ohmasa, M. Suzuki, and Y. Takéuchi, *Mineralogical Journal* 8 (1977): 311–319.

58. B. Y. S. R. Hall, J. M. Stewart, C. Hall, S. W. Mines, V. Island, and I. Ui, *Acta Crystallographica Section B: Structural Crystallography and Crystal* B29 (1973): 579.

59. R. Couderc, M. Amara, J. Degoulange, F. Madon, J. Fournier, and O. Le Corre, *Energy Procedia* 124 (2017): 470–477.

60. D. O. Scanlon, C. W. Dunnill, J. Buckeridge, et al., *Nature Materials* 12 (2013): 798–801.

61. O. Yepsen, J. Yáñez, and H. D. Mansilla, *Solar Energy* 171 (2018): 106–111.

62. T. Sekiya, T. Yagisawa, N. Kamiya, et al., *Journal of the Physical Society of Japan* 73 (2004): 703–710.

63. B. H. Lee, S. Park, M. Kim, et al., *Nature Materials* 18 (2019): 620–626.

64. S. L. J. Thomae, N. Prinz, T. Hartmann, M. Teck, S. Correll, and M. Zobel, *Review of Scientific Instruments* 90 (2019): 43905.

Supporting Information

Additional supporting information can be found online in the Supporting Information section.